

# Mechanically-Guided Deterministic Assembly of 3D Mesostructures Assisted by Residual Stresses

Haoran Fu, Kewang Nan, Paul Froeter, Wen Huang, Yuan Liu, Yiqi Wang, Juntong Wang, Zheng Yan, Haiwen Luan, Xiaogang Guo, Yijie Zhang, Changqing Jiang, Luming Li, Alison C. Dunn, Xiuling Li, Yonggang Huang, Yihui Zhang,\* and John A. Rogers\*

**F**ormation of 3D mesostructures in advanced functional materials is of growing interest due to the widespread envisioned applications of devices that exploit 3D architectures. Mechanically guided assembly based on compressive buckling of 2D precursors represents a promising method, with applicability to a diverse set of geometries and materials, including inorganic semiconductors, metals, polymers, and their heterogeneous combinations. This paper introduces ideas that extend the levels of control and the range of 3D layouts that are achievable in this manner. Here, thin, patterned layers with well-defined residual stresses influence the process of 2D to 3D geometric transformation. Systematic studies through combined analytical modeling, numerical simulations, and experimental observations demonstrate the effectiveness of the proposed strategy through  $\approx 20$  example cases with a broad range of complex 3D topologies. The results elucidate the ability of these stressed layers to alter the energy landscape associated with the transformation process and, specifically, the energy barriers that separate different stable modes in the final 3D configurations. A demonstration in a mechanically tunable microbalance illustrates the utility of these ideas in a simple structure designed for mass measurement.

Dr. H. Fu, Y. Liu, Dr. X. Guo  
Center for Mechanics and Materials  
AML  
Department of Engineering Mechanics  
Tsinghua University  
Beijing 100084, P. R. China

K. Nan, J. Wang, Y. J. Zhang, Prof. A. C. Dunn  
Department of Mechanical Science and Engineering  
University of Illinois at Urbana–Champaign  
Urbana, IL 61801, USA

P. Froeter, W. Huang, Prof. X. Li  
Department of Electrical and Computer Engineering  
Micro and Nanotechnology Laboratory  
International Institute for Carbon-Neutral Energy Research (IzCNER)  
University of Illinois at Urbana–Champaign  
Urbana, IL 61801, USA

Y. Wang, Dr. Z. Yan  
Department of Materials Science and Engineering  
Frederick Seitz Materials Research Laboratory  
University of Illinois at Urbana–Champaign  
Urbana, IL 61801, USA

H. Luan, Prof. Y. Huang  
Departments of Civil and Environmental Engineering  
Mechanical Engineering, and Materials Science and Engineering  
Northwestern University  
Evanston, IL 60208, USA

Dr. C. Jiang, Prof. L. Li  
Man-Machine-Environment Engineering Institute  
Department of Aeronautics & Astronautics Engineering  
Tsinghua University  
Beijing 100084, P. R. China



DOI: 10.1002/sml.201700151

## 1. Introduction

3D micro-/nanostructures are of growing interest, owing to their potential applications in areas from metamaterials,<sup>[1–7]</sup> to biomedical sensing devices,<sup>[8–16]</sup> to micro-electromechanical components,<sup>[17]</sup> to energy storage systems,<sup>[16,18–25]</sup> to electronics,<sup>[26–33]</sup> and to photonics and optoelectronics.<sup>[34–37]</sup> 3D mesostructures in advanced materials can be achieved using methods such as printing/writing,<sup>[38–41]</sup> fluidic self-assembly,<sup>[42,43]</sup> and templated growth.<sup>[44–47]</sup> Although these approaches offer many attractive features, most require specially designed chemistries,<sup>[38–41,48,49]</sup> and they cannot be used directly with many advanced functional materials of interest (e.g., single-crystalline semiconductors). Other routes that exploit capillary forces,<sup>[50–52]</sup> residual stresses,<sup>[33,53–58]</sup> or origami-inspired reconfigurable designs<sup>[59–62]</sup> offer compatibility with established planar device technologies. The former two are irreversible and have limited control over critical parameters such as the folding angle;<sup>[14,63–68]</sup> the latter one has been applied mainly to certain classes of geometries such as polyhedrons, tubes, and variants of these.

Methods based on compressive buckling<sup>[29,69–71]</sup> can transform 2D precursors built with nearly any class of thin film materials, including those used in the electronics and optoelectronics industries, into tunable 3D structures with diverse topologies. The process occurs in a parallel fashion at high throughput, over length scales from submicron to several centimeters. The 2D-to-3D transformation involves not only in- and out-of-plane translations and rotations, but also mechanical deformations dominated by out-of-plane bending and twisting, through design of the characteristics of the 2D precursors.<sup>[29,71,72]</sup> In most cases, unique 3D geometries result by consequence of strain energies in the first-order buckling modes (i.e., energetically the most probable configuration) that are much lower (e.g., by a factor of 2) than those of all other modes.<sup>[29]</sup> For certain complex 2D precursors, particularly those that yield 3D geometries with multilevel features, the strain energies of the first- and second-order (or higher-order) modes can be sufficiently similar to allow controlled access to a selected mode by use of external perturbation. The ideas introduced here exploit patterned thin films with

well-defined residual stresses, incorporated at strategic locations in the 2D precursor, as a means for this selection to achieve high-order ( $\geq 2$ ) buckling modes unobtainable previously, or for reconfiguration of local regions to achieve topologies qualitatively different from any of the buckling modes. The addition of these stress-controlling layers also can eliminate near degeneracies that sometimes occur between the lowest order mode and other modes of complex 3D configurations, thereby enhancing the yields in realizing targeted outcomes. The following text introduces the underlying mechanics issues through combined analytical modeling, numerical simulations, and experimental measurements. Demonstrations include a broad set of 3D mesostructures, each achieved using quantitative modeling/simulations to guide the choices of stresses and geometrical layouts of the control layers. An application in a mechanically tunable microbalance device serves as a simple example of the utility of these strategies in mass measurement of microscopic particles.

## 2. Results and Discussion

### 2.1. Fabrication Scheme and Design Principle

The overall approach for mechanically guided assembly of 3D mesostructures is similar to that reported recently,<sup>[29,69]</sup> in which 2D precursors typically formed by methods of semiconductor processing bond at selected locations onto prestretched elastomer substrates. The 3D structures result from coordinated motions induced by release of prestrain in the elastomer. For cases reported here, the precursors and bonding sites consist of photodefinable epoxy (SU8, thickness = 1.5–7  $\mu\text{m}$ ) and silicon oxide (thickness = 50 nm, via electron-beam evaporation). Patterned sacrificial layers (AZ5214, thickness = 1.4  $\mu\text{m}$ ) that are removed by immersion in acetone immediately prior to the buckling process ensure that the nonbonding regions separate efficiently from the elastomer. Here, the major differences in fabrication between the current and previous studies are in the preparation of thin films with well-defined residual stress, and in the adhesion of the residual-stress layers with selective region of 2D precursor. The stress-controlling layers consist of thin films of silicon nitride ( $\text{SiN}_x$ ) deposited with either tensile or compressive residual stresses, and patterned into desired geometries on the top surfaces of the 2D precursors by photolithography and reactive ion etching with  $\text{CF}_4$  gas (e.g., the 3D mesostructure shown in **Figure 1a**). Plasma-enhanced chemical vapor deposition (PECVD) of the  $\text{SiN}_x$  with control over parameters such as the direct current power, chamber pressure, gas flow rate, and operational frequency allows formation of thin films with well-defined residual stresses ranging from +480 to –581 MPa (+ and – indicates tensile and compressive residual stress, respectively; see Figure S1 in the Supporting Information for details). A thin layer of adhesive (Omni-coat, Microchem) cast on top of the SU8 before photopatterning ensures strong bonding between the  $\text{SiN}_x$  and SU8. Removing a layer of gold (thickness = 100 nm by electron beam evaporation) that is pre-deposited on silicon wafer as a sacrificial layer with wet etching (potassium iodide-iodine

---

Prof. Y. H. Zhang  
Center for Mechanics and Materials  
AML  
Department of Engineering Mechanics  
Tsinghua University  
Beijing 100084, P. R. China  
E-mail: yihuizhang@tsinghua.edu.cn

Prof. J. A. Rogers  
Departments of Materials Science and Engineering  
Biomedical Engineering  
Neurological Surgery  
Chemistry, Mechanical Engineering, Electrical Engineering  
and Computer Science  
Simpson Querrey Institute and Feinberg Medical School  
Center for Bio-Integrated Electronics  
Northwestern University  
Evanston, IL 60208, USA  
E-mail: jrogers@northwestern.edu

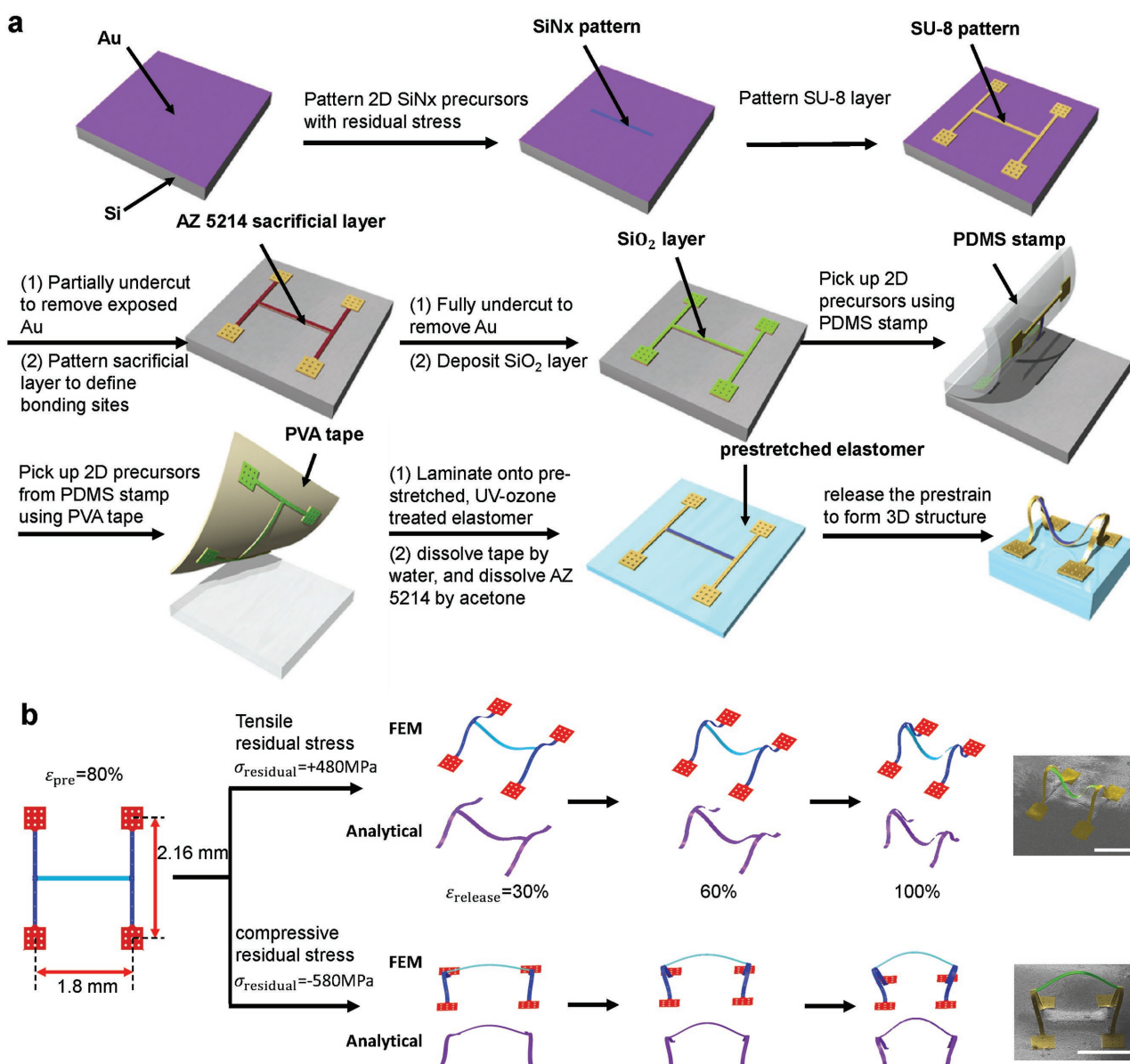


**Figure 1.** a) Schematic illustration of steps for fabricating 3D mesostructures using controlled, compressive buckling assisted by residual stresses. b) Results of experiment, analytical modeling, and FEA predictions for the residual-stress assisted assembly from an H-shaped 2D precursor. Results of analytical modeling and FEA (middle three panels) describe the formation of the 3D mesostructure (SU8 and SiN<sub>x</sub>), along with corresponding SEM images (right most panel) of the final configuration. Scale bars, 1 mm.

complex (KI-I<sub>2</sub>) etchant) allows release of the SU8/SiN<sub>x</sub> patterns for transfer. Detailed fabrication procedures are in Figure 1a, the Experimental Section, and Figure S2 (Supporting Information).

Figure 1b presents an example of residual-stress assisted assembly of two-floor mesostructures from an H-shaped 2D precursor, whose base consists of a single layer of SU8 with uniform thickness (2 μm) and bonding sites indicated in red. SiN<sub>x</sub> resides only on top of the central ribbon (100 nm SiN<sub>x</sub>/2 μm SU8) to leverage the strain mismatch for controlling its bending direction during assembly. Compressive forces associated with the substrate prestrain ( $\epsilon_{\text{pre}} = 80\%$ ) act in combination with those associated with the residual stresses in the SiN<sub>x</sub> to transform the 2D precursor into controlled 3D configurations. Intermediate states in the

assembly process, denoted by the magnitude of released strain (Figure S3, Supporting Information), can be obtained from finite element analysis (FEA) and analytical modeling (see Figure S4 and the text in the Supporting Information for details), as shown in Figure 1b. When the SiN<sub>x</sub> layer has a sufficiently large tensile residual stress (e.g., +480 MPa), the center ribbon tends to bend downward to minimize the strain energy. In contrast, this ribbon bends upward without the SiN<sub>x</sub>, or with a layer of SiN<sub>x</sub> that has compressive stress (e.g., -580 MPa) or tensile stress below a certain threshold. In both cases, the final 3D configurations predicted by FEA or analytical modeling agree well with the scanning electron microscope (SEM) images from experiments.

The bending direction (up or down) can be controlled by the residual stress ( $\sigma_{\text{residual}}$ ), the thickness ( $t_{\text{SiN}_x}$ ) of the

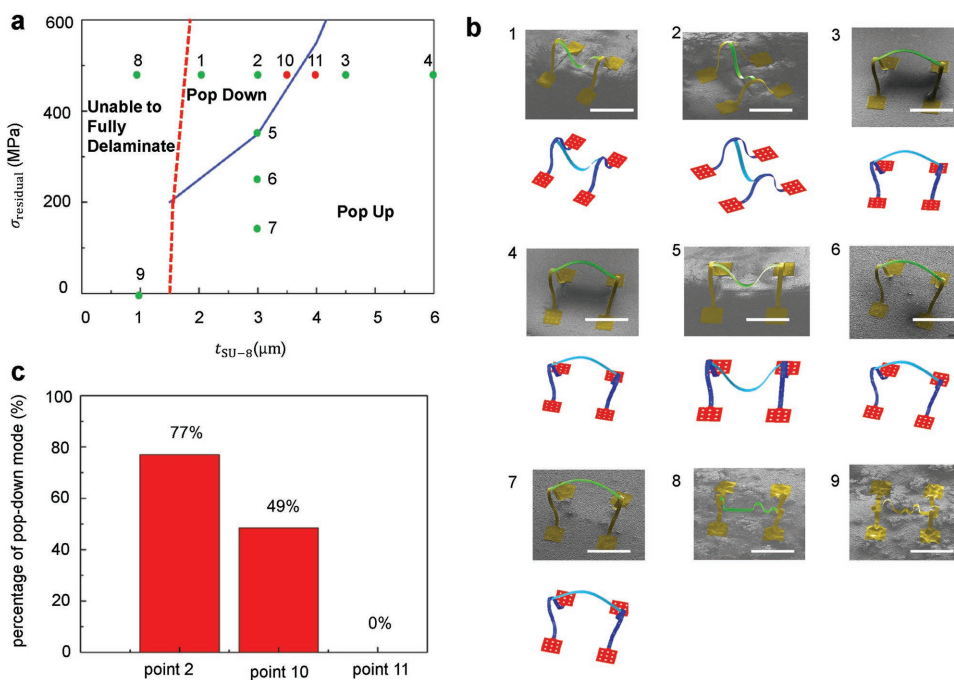


**Figure 2.** a) Design diagram in the space of residual stress ( $\sigma_{\text{residual}}$ ) and SU8 thickness ( $t_{\text{SU8}}$ ), for  $t_{\text{SiN}_x} = 100$  nm. b) SEM images and corresponding FEA predictions for 3D mesostructures with different design parameters as marked by the circles in (a). c) Probability to achieve pop-down mode for 2D precursors with three different design parameters (corresponding to points “2,” “10,” and “11” in (a)). Scale bars, 1 mm.

$\text{SiN}_x$ , and the thickness ( $t_{\text{SU8}}$ ) of the SU8. **Figure 2a** presents a design diagram in the space of  $\sigma_{\text{residual}}$  and  $t_{\text{SU8}}$  for a given  $\text{SiN}_x$  thickness ( $t_{\text{SiN}_x} = 100$  nm). Three different domains, denoted by “pop-up,” “pop-down,” and “unable to fully delaminate,” can be identified. Here, to achieve full delamination of the 2D precursor from the substrate,  $t_{\text{SU8}}$  must be sufficiently large to provide separation forces that can overcome the van der Waals interactions at the weak interface with the substrate. Such interactions result mainly from the collapse of the freestanding 2D ribbons onto the substrate after removal of the thin sacrificial layers (1.4  $\mu\text{m}$ ). The critical thickness for full delamination, as represented by the red dashed line in Figure 2a, can be estimated quantitatively using an energetic analysis (see Figure S5 and the text in the Supporting Information for details). FEA results define the boundary between the two different buckling modes, as shown by the blue solid line in Figure 2a. The minimum tensile residual stress necessary to achieve the pop-down buckling mode increases with increasing SU8 thickness. For small stresses, the pop-up buckling mode occurs. Experimental results based on precursors with various different geometries appear as circles (numbered from “1” to “9”) in Figure 2a. Representative 3D configurations shown in the SEM images of Figure 2b agree well with the FEA predictions and the design diagram. The configurations of structures (points “8” and “9”) that do not delaminate fully are sensitive to subtle properties of the interface with the substrate, and are therefore difficult to predict by modeling. Experiments and FEA indicate that the final 3D configurations for a given buckling mode (pop-down or -up) are insensitive to changes in  $\sigma_{\text{residual}}$  and  $t_{\text{SU8}}$ , for the ranges considered herein.

Even for parameters that correspond to the “pop-down” domain in Figure 2a, the pop-up mode is still possible,

because it corresponds to a local minimum in the strain energy minimum, as detailed in the subsequent section. The variability likely arises from slight differences in experimental conditions, such as asynchronous release of the biaxial strain and/or parasitic adhesion/stiction at regions adjacent to the bonding sites. A statistical analysis based on observations from sample (>30)s with, nominally, the same design parameters illustrates this effect. A representative set of results appear in Figure S6 (Supporting Information) for the design point “10” ( $\sigma_{\text{residual}} = +480$  MPa and  $t_{\text{SU8}} = 3.5$   $\mu\text{m}$ ). The data indicate that the probability of the pop-down mode is  $\approx 49\%$ . The results in Figure 2c show that the probability of the pop-down mode decreases sharply as the location of the design parameter moves gradually from the domain of “pop-down” to “pop-up.”

## 2.2. Mechanics of Buckling Mode Control

Energetic analyses capture the underlying mechanics of buckling mode control. Three representative examples have the design parameters ( $t_{\text{SU8}}, t_{\text{SiN}_x}, \sigma_{\text{residual}}$ ) = (3  $\mu\text{m}$ , 100 nm, 480 MPa), (3.5  $\mu\text{m}$ , 100 nm, 480 MPa), and (4  $\mu\text{m}$ , 100 nm, 480 MPa), respectively, corresponding to points “2,” “10,” and “11” in Figure 2a. All calculations use a prestrain  $\epsilon_{\text{pre}} = 80\%$ .

**Figure 3a,b** depicts the dependence of strain energy on the released strain ( $\epsilon_{\text{release}}$ ) for the case with design parameters (3  $\mu\text{m}$ , 100 nm, 480 MPa). According to the result in Figure 2c, both pop-down and pop-up modes are possible with this set of parameters. The tensile residual stress in the  $\text{SiN}_x$  layer, however, causes the pop-down mode to have a lower strain energy than the pop-up mode at the initial stage of strain release (e.g.,  $\epsilon_{\text{release}} = 0\text{--}7.5\%$ ). As a consequence,

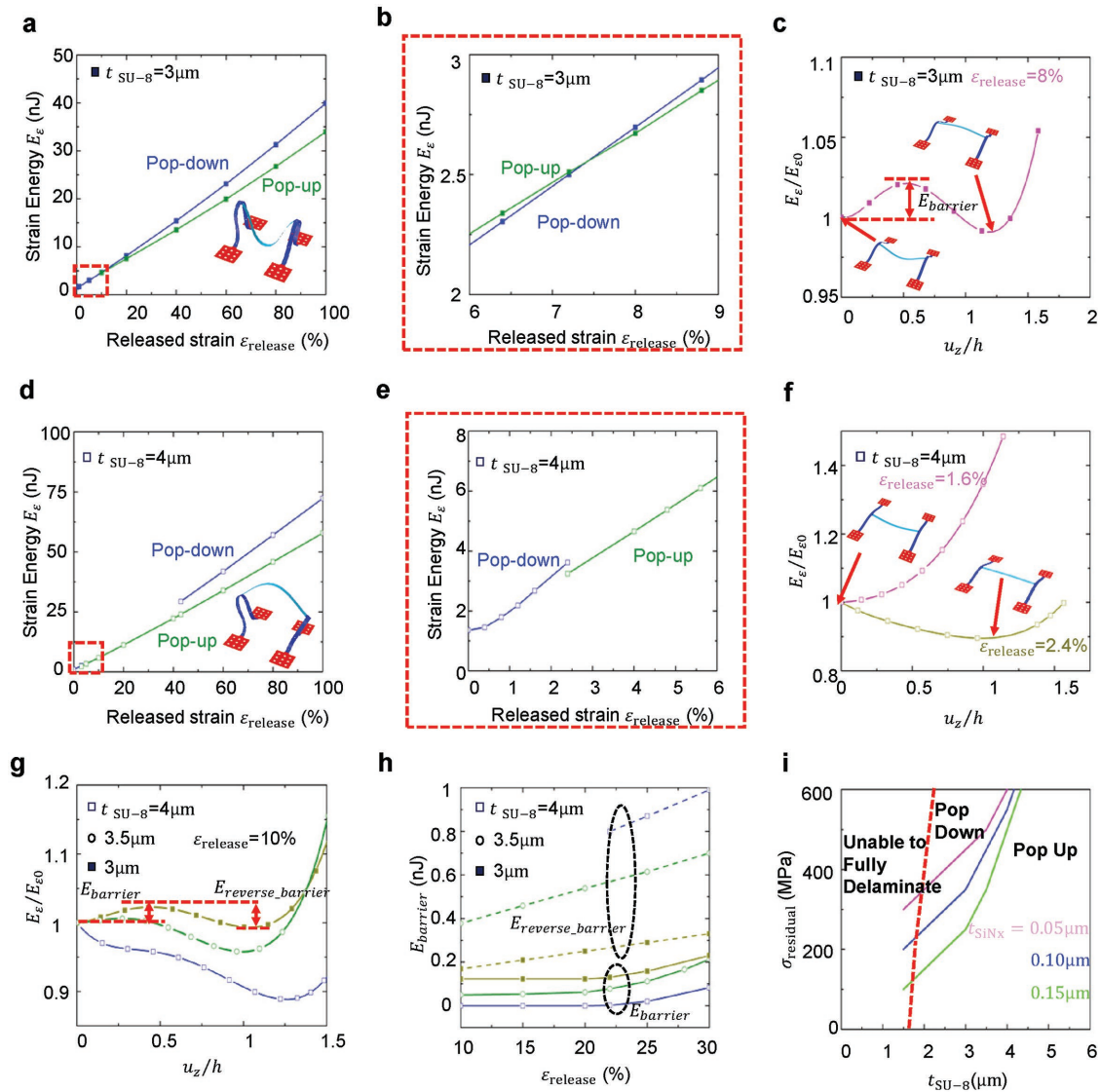


**Figure 3.** Mechanics analyses of buckling mode control for the H-shaped 2D precursor. Strain energy of 3D structures with pop-up (blue) and pop-down (green) modes versus released strain, and the corresponding magnified view, for the design parameters  $(t_{\text{SU8}}, t_{\text{SiNx}}, \sigma_{\text{residual}}) = \text{a,b}) (3 \mu\text{m}, 100 \text{ nm}, 480 \text{ MPa})$  and  $\text{d,e}) (4 \mu\text{m}, 100 \text{ nm}, 480 \text{ MPa})$ . The insets of (a) and (d) show the corresponding final 3D configurations. **c,f)** Normalized strain energy versus out-of-plane displacement for  $(t_{\text{SU8}}, t_{\text{SiNx}}, \sigma_{\text{residual}}, \epsilon_{\text{release}}) = (3 \mu\text{m}, 100 \text{ nm}, 480 \text{ MPa}, 7.5\%), (4 \mu\text{m}, 100 \text{ nm}, 480 \text{ MPa}, 1.6\%),$  and  $(4 \mu\text{m}, 100 \text{ nm}, 480 \text{ MPa}, 2.4\%)$ , with the insets showing the stable buckling modes at the corresponding released strains. Here,  $h$  is the out-of-plane dimension of the first-floor structure, and it varies with changing the released strain. **g)** Normalized strain energy versus out-of-plane displacement for  $(t_{\text{SiNx}}, \sigma_{\text{residual}}, \epsilon_{\text{release}}) = (100 \text{ nm}, 480 \text{ MPa}, 10\%)$  and three different SU8 thicknesses. **h)** Strain energy barrier versus released strain for  $(t_{\text{SiNx}}, \sigma_{\text{residual}}, \epsilon_{\text{release}}) = (100 \text{ nm}, 480 \text{ MPa}, 10\%)$  and three different SU8 thicknesses. **i)** Design diagram in the space of residual stress ( $\sigma_{\text{residual}}$ ) and SU8 thickness ( $t_{\text{SU8}}$ ), for  $t_{\text{SiNx}} = 50, 100,$  and  $150 \text{ nm}$ . The geometric dimensions of the 2D precursor are the same as that in Figure 1, and the prestrain adopted in the analyses is 80%.

the structure tends to move into the pop-down mode. As the released strain increases beyond 7.5%, the strain energy of pop-down mode exceeds that of the pop-up mode. The buckling mode is, however, unable to transform into the pop-up mode, due to the existence of an energy barrier, as shown in Figure 3c and Figure S7 (Supporting Information). The magnitude of this barrier as a function of  $\epsilon_{\text{release}}$  can be obtained by applying an out-of-plane displacement  $u_z$  at the middle point of the bilayer until the mode switches from pop-down to pop-up, as illustrated in Figure S7 (Supporting Information). During this process, the strain energy first increases to a maximum, and then decreases with increasing  $u_z$ , as shown

in Figure 3c for  $\epsilon_{\text{release}} = 8\%$ . The difference between the maximum strain energy and the initial value for  $\epsilon_{\text{release}} = 0\%$  is simply the energy barrier ( $E_{\text{barrier}}$ ) of interest. For design parameters  $(3 \mu\text{m}, 100 \text{ nm}, 480 \text{ MPa})$ , such a barrier exists during the entire process of strain release (Figure 3h). Here, the double energy wells result in two stable states. Nevertheless, due to an inability to overcome the energy barrier ( $E_{\text{barrier}}$ ), the 3D structure maintains the pop-down mode as the released strain increases.

The design parameters  $(4 \mu\text{m}, 100 \text{ nm}, 480 \text{ MPa})$  lead to a different characteristic variation in the strain energy, as shown in Figure 3d–f. Here, for  $\epsilon_{\text{release}} = 0\text{--}2.4\%$ , the

pop-down mode corresponds to the only stable buckling mode, due to the single energy well in Figure 3f. As the  $\epsilon_{\text{release}}$  increases beyond 2.4%, the pop-down mode transforms into the pop-up mode which corresponds to the single energy minimum in Figure 3f (i.e., with zero energy barrier,  $E_{\text{barrier}} = 0$ ).

These observations indicate that the buckling mode is mainly governed by the existence of an energy barrier. External energy input can, however, overcome this barrier, leading to a transformation between the two different modes. The probability of transformation is directly related to the magnitude of the barrier, as confirmed in Figure 3g,h. Specifically, the non-zero energy barrier of point “2” in Figure 2a is larger than that of point “10,” indicating a high probability to maintain the pop-down mode. The reverse energy barrier of point “2” is lower than that of point “10” (Figure 3g), indicating a high probability to switch back to pop-down mode if the structure is in the pop-up mode, consistent with the experimental results in Figure 2c. Meanwhile, because the energy barrier of point “11” in Figure 2a is zero for  $\epsilon_{\text{release}}$  in the range of 10%–20%, the structure spontaneously transforms into the pop-up mode. Moreover, its reverse energy barrier is much larger than the other two points, leading to a lower probability to transform back, consistent with the experimental results in Figure 2c. Figure 3i presents an extended design diagram of Figure 2a that accounts for the influence of  $\text{SiN}_x$  thickness. The results show that the magnitude of the residual stress required to achieve a pop-down mode decreases with increasing the  $\text{SiN}_x$  thickness for ranges (e.g., from 0 to 400 nm) of interest here.

### 2.3. Complex Hierarchical 3D Mesostructures with Deterministic Buckling Modes

With this model of the mechanics as a guide, a broad set of complex hierarchical 3D structures with different buckling modes can be assembled in a deterministic manner, with the aid of residual stresses. **Figure 4** and Figure S8 (Supporting Information) present FEA predictions and experimental results for ten complex mesostructures in SU8 (5  $\mu\text{m}$ ), each of which incorporates stress-controlling layers of  $\text{SiN}_x$  (100 nm), along with the designs of the corresponding 2D precursors. The top left frame of Figure 4a presents a precursor that includes four triangles with centroids of each connected by three ribbons (denoted by groups ① ② ③ ④) without any  $\text{SiN}_x$ . The six small hexagons (red) adhere strongly to a biaxially prestrained elastomeric substrate. After relaxing the prestrain, the ribbons of groups ① ② ③ pop up, while those of group ④ pop down, corresponding to mode I. The addition of  $\text{SiN}_x$  layers with compressive residual stress ( $\sigma_{\text{residual}} = -580$  MPa, dark yellow) to local regions of the precursor switches the bending direction of the associated ribbons. For example, when  $\text{SiN}_x$  layers are on all the ribbon groups (① ② ③ ④), then all of the relevant ribbons pop up, corresponding to mode II (Figure 4a, middle). With  $\text{SiN}_x$  layers only on ribbons of group ④, those ribbons pop up while the ribbons of other groups pop down (mode III, bottom row of Figure 4a). Figure 4b shows the design diagram for this set

of 3D structures, in which the red dashed line indicates the minimum SU8 thickness for full delamination. The blue and pink lines are the boundaries between mode I and mode II and between mode I and mode III.

Figure 4c shows a 3D mesostructure with a triple-floor architecture that corresponds to a 2D precursor without any  $\text{SiN}_x$  (Figure 4c, left top).<sup>[29]</sup> The material composition is almost identical to that of structures in Figure 4a, except for the addition of a layer of gold (30 nm) to enhance visibility under an optical microscope. The ribbons ① ② undergo an additional level of buckling to form an elevated “second floor,” while ribbon ③ forms the third floor (Figure 4c, top). With the addition of  $\text{SiN}_x$  layers (tensile residual stress,  $\sigma_{\text{residual}} = +480$  MPa, indigo), the third floor can either deform in an asymmetric manner (Figure 4c, middle) or pop down (Figure 4c, bottom). In addition to the locations of the  $\text{SiN}_x$  layers, the sign of the residual stress also plays a crucial role. Figure S8 (Supporting Information) indicates that with the same 2D precursor and  $\text{SiN}_x$  layers, tensile and compressive residual stresses yield distinct 3D configurations (the last two modes), both of which differ from the case without  $\text{SiN}_x$  (the first mode). In all of the above examples, experimental results show excellent agreement with FEA predictions, thereby establishing the computational models as reliable tools for rapid design optimization.

### 2.4. Application in a Mechanically Tunable Microbalance Device

The ability to control 3D geometries, including the shapes of local regions, represents an attractive feature of the addition of stress-controlling layers. **Figure 5a–e** provides a simple device demonstration in the form of a tunable microbalance for mass measurement. The design of the 2D precursor appears in Figure 5a. The part in indigo consists of a bilayer of  $\text{SiN}_x$  (100 nm) and SU8 (5  $\mu\text{m}$ ), and the other part (blue and red) consists of a single-layer SU8 (10  $\mu\text{m}$ ). A tensile residual stress of 480 MPa in the  $\text{SiN}_x$  layer ensures that the central part (indigo) pops down during assembly to facilitate the placement of microscale object to be measured. Fully releasing the prestrain in the substrate results in a 3D structure with a flat plate in the center (Figure 5b). A small mass (e.g., a few milligrams to tens of milligrams) placed on the plate deforms the structure downward by an amount that can be recorded by a nanoindenter (Figure S9, Supporting Information) or other metrology tool. The relationship between mass and displacement can be calibrated by experimental results and numerical simulations. Figure 5c illustrates a linear relationship between the displacement and mass. The upper limit of the measurement range corresponds to the mass needed to initiate physical contact between the plate and the substrate. FEA results in Figure 5d,e demonstrate that this limit can be adjusted by changing the prestrain, or equivalently, by stretching the underlying substrate after 3D assembly. This type of device might find use in microfluidic systems for monitoring and separation of colloidal silica microparticles with the radius on the order of hundreds of microns.<sup>[73,74]</sup>

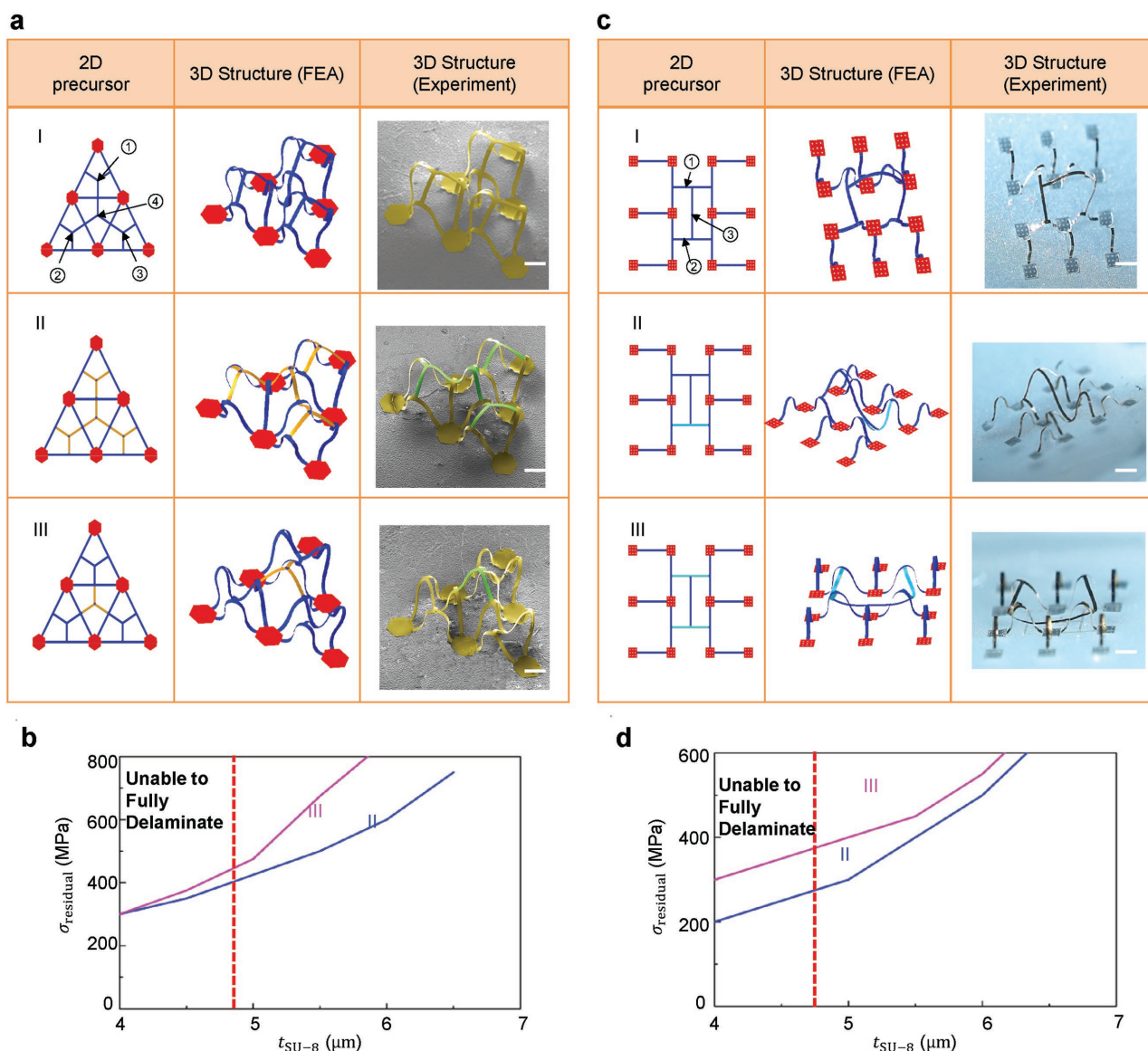


**Figure 4.** 3D mesostructures formed through the approach of compressive buckling assisted by residual stresses. a) 2D precursors, FEA predictions, and SEM images for triangular ribbon networks made of  $\text{SiN}_x$  and polymer (SU8). b) Design diagram of triangular ribbon networks in the space of residual stress ( $\sigma_{\text{residual}}$ ) and SU8 thickness ( $t_{\text{SU-8}}$ ) for selection of different buckling modes. c) 2D precursors, FEA predictions, and optical images for triple-floor structures made of  $\text{SiN}_x$  and bilayers of gold and polymer (SU8). d) Design diagram of triple-floor structures in the space of residual stress ( $\sigma_{\text{residual}}$ ) and SU8 thickness ( $t_{\text{SU-8}}$ ) for selection of different buckling modes. Scale bars, 500  $\mu\text{m}$ .

### 2.5. Assembly of 3D Structures with Geometries Previously Inaccessible

The same residual-stress strategy can also enable formation of complex structures with 3D topologies that differ qualitatively from any of the buckling modes. Here, the utility of patterned shape memory polymers (SMPs) as a means for introducing the stresses provide examples complementary to those achievable with  $\text{SiN}_x$ . Specifically, as detailed in the Experimental Section, the SMP layers can involve large residual strains ( $\approx 20\%$ , corresponding to  $\approx 16$  MPa residual stress at 100  $^\circ\text{C}$ ), and thicknesses ( $>60 \mu\text{m}$ ), sufficient for forces that can govern the 3D transformation of targeted regions of a 2D precursor. To demonstrate the diversity of applicable material classes for

this deterministic assembly strategy, a bilayer of Cu (thickness = 1  $\mu\text{m}$ )/Polyethylene terephthalate (PET, thickness = 50  $\mu\text{m}$ ) (blue) served as the basis for the formation of 3D structures. **Figure 6** presents FEA predictions and millimeter-scale experiments achieved with 2D precursors in a bilayer of Cu/PET (blue) with SMP layers (thickness = 100  $\mu\text{m}$ ) at strategically designed regions. Here, the SMP layer can adhere to the precursor on the top (indigo) or the bottom (dark yellow). Detailed fabrication procedures are in the Experimental Section and Figure S10 (Supporting Information).

Figure 6a presents a complex 3D table structure assembled through global buckling and local rolling of the 2D precursor. Here, the rolling follows from the mismatch strain between the SMP and other layers upon heating in water

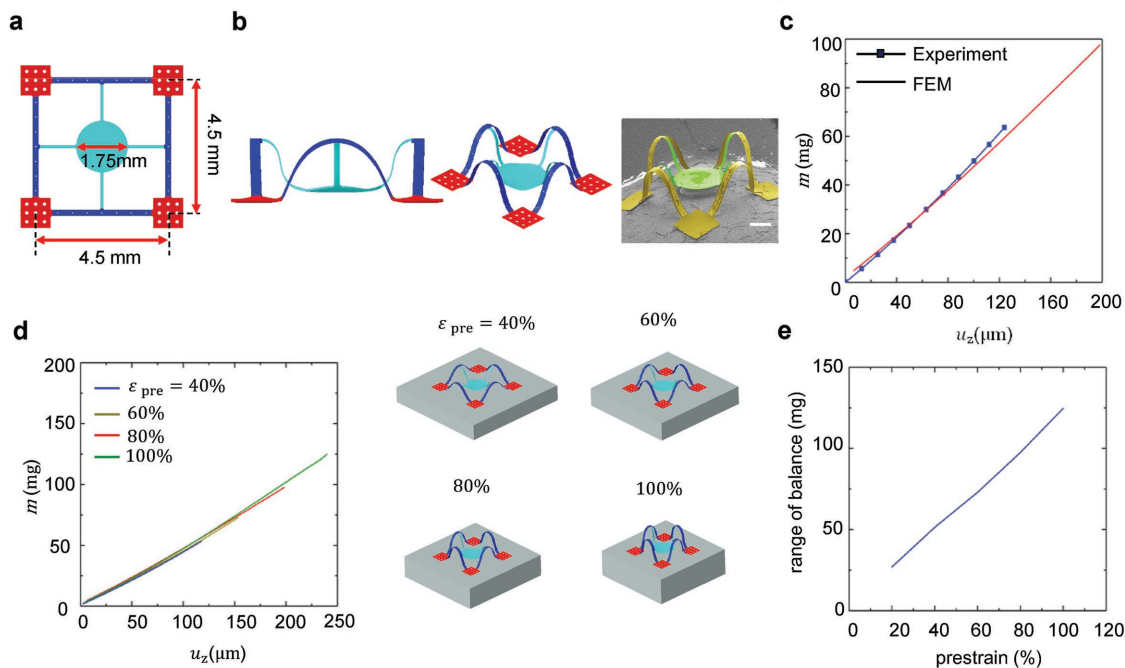


**Figure 5.** A simple, mechanically tunable microbalance device. a) 2D precursor for the device. b) FEA prediction and SEM images from two different viewing angles. c) Measured and computed dependence of the mass on the vertical displacement. d) Mass versus vertical displacement for devices assembled with four different levels of prestrain, along with their corresponding 3D configurations. e) The range of the microbalance as a function of the prestrain. Scale bars, 500  $\mu\text{m}$ .

(100 °C), leading to formation of four circular rings on top of the buckled table (Figure 6a, right bottom). Unlike examples described previously, this hybrid 3D configuration does not correspond to any of the buckling modes of the 2D precursor without the SMP. Figure 6b shows a hierarchical 3D structure in the form of three square membranes decorated symmetrically with 12 circular rings. This class of architectures with lifted circular rings could be further combined with semiconductor techniques to achieve optoelectronic applications, for example, as optical ring resonators that offer signal processing and communication at an enhanced efficiency.<sup>[75]</sup>

Coupled compressive buckling and stress-induced bending are also possible with appropriate designs of 2D precursors. Two examples appear in Figure 6c,d, both of which adopt a straight ribbon design with nonuniform widths and leverage residual stresses in the SMP layer to control the folding direction at localized regions for multiple folds. In the first case (Figure 6c, left), the SMP layers exist at five narrow regions in the ribbon, with two on the top (indigo) and the other three on the bottom side (dark yellow). The ribbon pops up into an arc via global compressive buckling (Figure 6c, right top) after release of prestrain in the elastomeric substrate. This arc then reshapes into a wavy structure with five folds (Figure 6c, right bottom) after activating the SMP. The second design in Figure 6d uses a 2D precursor similar to that of Figure 6c, except for the distribution of SMP layers (Figure 6c, left). The final 3D structure corresponds to a wavy pattern with three folds (Figure 6d, right bottom). In all cases, the 3D configurations predicted by FEA agree well with experimental results.

### 3. Conclusion

In summary, this paper introduces residual stresses as a design strategy enhancement for buckling-guided approaches to deterministic assembly of multilevel 3D mesostructures. Combined numerical simulations and experimental observations reveal the underlying physics and design considerations. With carefully configured residual-stress layers and judicious selection of layout parameters, complex buckling modes with previously inaccessible 3D topologies can be achieved. In one simple case, a 3D structure that incorporates a platform with a highly linear displacement–mass relationship provides a basic example in microbalance based mass measurement, with a tunable range. In a complementary set of structures, residual stress not only controls the buckling mode, but imparts sufficient forces to create entirely differentiated 3D geometries. The material systems presented here, i.e.,  $\text{SiN}_x$  and SMP, represent a small fraction of the possibilities that could be considered, such as environmentally responsive systems.

### 4. Experimental Section

#### *Fabrication of Micrometer-Scale 3D Structure with $\text{SiN}_x$ Layer:*

Electron beam evaporation formed a bilayer of 5 nm of chromium and 100 nm of gold on a clean silicon wafer at pressures between 0.7 and 3.4  $\mu\text{Torr}$ , and at rates of 0.5–0.7 and 0.9–1.2  $\text{\AA s}^{-1}$ , respectively. Following deposition, loading the wafer into a dual-frequency PECVD tool enabled deposition of 100 nm of  $\text{SiN}_x$ , either at high or low frequencies to generate films with tensile or compressive stresses, respectively. Specifically, tensile stress follows

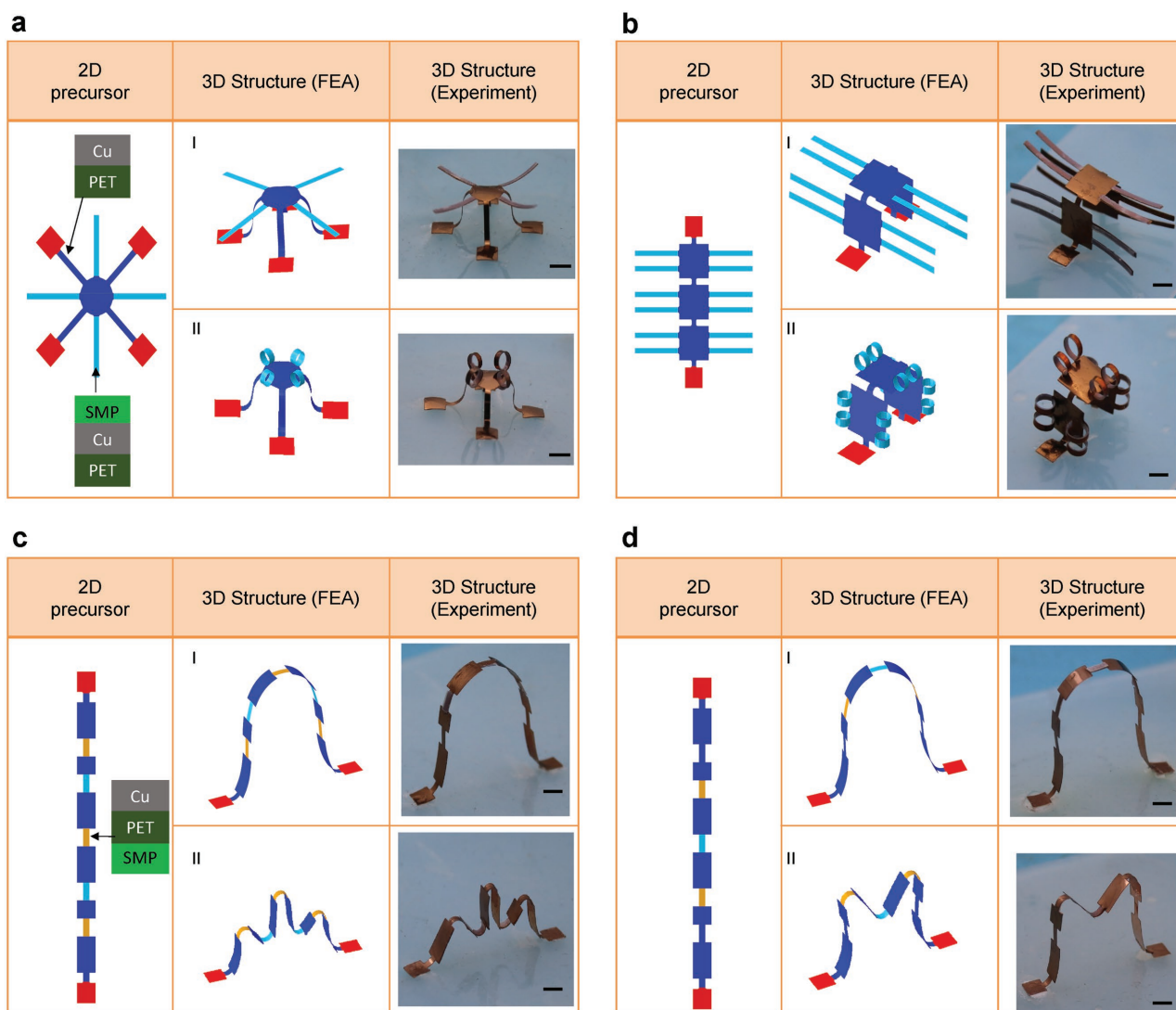


**Figure 6.** 3D millimeter-scale structures formed through the use of shape memory polymers (SMP). a) 2D precursors, FEA predictions, and optical images for a complex 3D table structure made of SMP and bilayers of copper and PET. The structure here is formed in a way that compressive buckling and stress-induced bending work independently. The results in the top and bottom rows represent the 3D configuration before and after releasing the prestrain in SMP, respectively. b) Similar results for a hierarchical 3D structure. c,d) Similar results for two structures with multiple folds formed by coupled compressive buckling and stress-induced bending. Scale bars, 5 mm.

from low density Si–N bonds that stretch to interact with each other, which occurs primarily under high frequency deposition condition; compressive stress follows from low-frequency and high-power conditions which result in excess amine and other fragments. Details of film chemistry and strain generation can be found elsewhere.<sup>[32,76]</sup> Photolithographically patterning AZ5214 photoresist and then etching away the exposed regions of the SiN<sub>x</sub> using CF<sub>4</sub> reactive ion etching, backstopped by the gold sacrificial layer, yielded desired geometries in the stressed layer. A barrel plasma etcher with O<sub>2</sub> gas at 500 W for 3 min removed the photoresist.

Spin-coating yielded a thin layer of adhesion promoter (Omnicot, Microchem) and an overlayer of a photodefinable epoxy (SU8, Microchem). Photopatterning the SU8 defined the target geometries. After a brief exposure to oxygen plasma to remove the exposed adhesion promoter, dipping the wafer into gold etchant (Type TFA, Transene) partially undercut the gold. Photolithography

with AZ5214 photoresist yielded a pattern to cover all regions of the SU8 except areas to define the bonding sites. Next, immersion in gold etchant overnight completely removed the gold layer, to allow retrieval of the structures (i.e., 2D precursors) using a polydimethylsiloxane (PDMS) stamp via transfer printing. Before transfer, thin layers of titanium (5 nm) and silicon dioxide (40 nm) deposited onto the precursors by electron beam evaporation created surface chemistry necessary for improved adhesion at the bonding sites. A water-soluble polyvinyl alcohol (PVA) tape enabled retrieval of the 2D precursors from the PDMS stamp, for subsequent lamination onto a UV-ozone treated, prestretched elastomer substrate (thickness = 0.4 mm, Dragon Skin, Smooth-on). After curing in a convection oven at 70 °C for 7 min, immersion in warm water dissolved the PVA tape. Exposure to an acetone bath for 20 min led to full undercut of the AZ5214 layer. Finally, slowly releasing the prestrain led to formation of the 3D structures.

A schematic illustration of the procedure appears in Figure S2 (Supporting Information).

**Fabrication of Millimeter-Scale 3D Structure with SMP Layer:** An automated cutting machine formed structures in bilayers of copper (1  $\mu\text{m}$ )/PET (50  $\mu\text{m}$ ). A commercial 3D printer (Stratasys Ltd.) served as a means to pattern the SMP in the form of two parallel ribbons (100  $\mu\text{m}$ ) connected to the cuboids at both ends (Figure S11, Supporting Information). Each layer formed in this way had a thickness of 16  $\mu\text{m}$ , and each of the 2D ribbons consisted of four or more layers. The printed structure was then prestretched uniaxially in hot water (100  $^{\circ}\text{C}$ ) for  $\approx 2$  min by 20%. After cooling the structure to room temperature, parallel ribbons of SMP were cut to required dimensions. Adhering the SMP layer to the copper/PET layer on the top or bottom side by a commercial adhesive (Super Glue, Gorilla Glue Company) completed the preparation of the 2D precursors.

A thin silicone substrate (2 mm in thickness, Dragon Skin) served as the assembly platform. Super Glue dispensed at desired locations on the 2D precursors resulted in strong bonding to the silicone substrate, after curing for  $\approx 10$  min at room temperature. Slowly releasing the prestrain in the substrate, with a strain rate of  $< 0.008 \text{ s}^{-1}$ , completed the assembly process. Placing the entire structure into hot water (100  $^{\circ}\text{C}$ ) released the prestrain in the SMP layer to reshape the 3D geometry defined by buckling.

## Supporting Information

Supporting Information is available from the Wiley Online Library or from the author.

## Acknowledgements

H.F. and K.N. contributed equally to this work. Y.Z. acknowledges the support from the National Natural Science Foundation of China (Grant No. 11672152) and the National Basic Research Program of China (Grant No. 2015CB351900). Work by J.A.R. and X.L. was supported by the U.S. Department of Energy (DOE), Office of Science, Basic Energy Sciences (BES) under Award #DEFG02-07ER46471. Y.H. acknowledges the support from the NSF (Grant Nos. DMR-1121262, CMMI-1300846, CMMI-1534120, and CMMI-1400169) and the NIH (Grant No. R01EB019337).

[1] J. Valentine, S. Zhang, T. Zentgraf, E. Ulin-Avila, D. A. Genov, G. Bartal, X. Zhang, *Nature* **2008**, *455*, 376.  
 [2] T. A. Schaedler, A. J. Jacobsen, A. Torrents, A. E. Sorensen, J. Lian, J. R. Greer, L. Valdevit, W. B. Carter, *Science* **2011**, *334*, 962.  
 [3] X. Zheng, H. Lee, T. H. Weisgraber, M. Shusteff, J. DeOtte, E. B. Duoss, J. D. Kuntz, M. M. Biener, Q. Ge, J. A. Jackson, S. O. Kuheyyev, N. X. Fang, C. M. Spadaccini, *Science* **2014**, *344*, 1373.  
 [4] D. Jang, L. R. Meza, F. Greer, J. R. Greer, *Nat. Mater.* **2013**, *12*, 893.  
 [5] J.-H. Cho, M. D. Keung, N. Verellen, L. Lagae, V. V. Moshchalkov, P. Van Dorpe, D. H. Gracias, *Small* **2011**, *7*, 1943.  
 [6] C. M. Soukoulis, M. Wegener, *Nat. Photonics* **2011**, *5*, 523.  
 [7] S. Yang, I.-S. Choi, R. D. Kamien, *MRS Bull.* **2016**, *41*, 130.

[8] B. Tian, J. Liu, T. Dvir, L. Jin, J. H. Tsui, Q. Qing, Z. Suo, R. Langer, D. S. Kohane, C. M. Lieber, *Nat. Mater.* **2012**, *11*, 986.  
 [9] A. Sidorenko, T. Krupenkin, A. Taylor, P. Fratzl, J. Aizenberg, *Science* **2007**, *315*, 487.  
 [10] R. Feiner, L. Engel, S. Fleischer, M. Malki, I. Gal, A. Shapira, Y. Shacham-Diamand, T. Dvir, *Nat. Mater.* **2016**, *15*, 679.  
 [11] V. Misra, A. Bozkurt, B. Calhoun, T. N. Jackson, J. S. Jur, J. Lach, B. Lee, J. Muth, O. Oralkan, M. Oeztuerk, S. Trolie-McKinstry, D. Vashae, D. Wentzloff, Y. Zhu, *Proc. IEEE* **2015**, *103*, 665.  
 [12] S. Yao, Y. Zhu, *JOM* **2016**, *68*, 1145.  
 [13] S. Yao, Y. Zhu, *Adv. Mater.* **2015**, *27*, 1480.  
 [14] T. G. Leong, C. L. Randall, B. R. Benson, N. Bassik, G. M. Stern, D. H. Gracias, *Proc. Natl. Acad. Sci. USA* **2009**, *106*, 703.  
 [15] G.-T. Hwang, M. Byun, C. K. Jeong, K. J. Lee, *Adv. Healthcare Mater.* **2015**, *4*, 646.  
 [16] H. G. Yoo, M. Byun, C. K. Jeong, K. J. Lee, *Adv. Mater.* **2015**, *27*, 3982.  
 [17] Y. Zhu, T.-H. Chang, *J. Micromech. Microeng.* **2015**, *25*, 093001.  
 [18] X. Xiao, W. Zhou, Y. Kim, I. Ryu, M. Gu, C. Wang, G. Liu, Z. Liu, H. Gao, *Adv. Funct. Mater.* **2015**, *25*, 1426.  
 [19] H. Wu, G. Yu, L. Pan, N. Liu, M. T. McDowell, Z. Bao, Y. Cui, *Nat. Commun.* **2013**, *4*, 1943.  
 [20] J. Deng, H. Ji, C. Yan, J. Zhang, W. Si, S. Baunack, S. Oswald, Y. Mei, O. G. Schmidt, *Angew. Chem., Int. Ed.* **2013**, *52*, 2326.  
 [21] K. Sun, T.-S. Wei, B. Y. Ahn, J. Y. Seo, S. J. Dillon, J. A. Lewis, *Adv. Mater.* **2013**, *25*, 4539.  
 [22] H. Zhang, X. Yu, P. V. Braun, *Nat. Nanotechnol.* **2011**, *6*, 277.  
 [23] R. Tang, H. Huang, H. Tu, H. Liang, M. Liang, Z. Song, Y. Xu, H. Jiang, H. Yu, *Appl. Phys. Lett.* **2014**, *104*, 083501.  
 [24] Z. Song, X. Wang, C. Lv, Y. An, M. Liang, T. Ma, D. He, Y.-J. Zheng, S.-Q. Huang, H. Yu, H. Jiang, *Sci. Rep.* **2015**, *5*, 10988.  
 [25] Z. Song, T. Ma, R. Tang, Q. Cheng, X. Wang, D. Krishnaraju, R. Panat, C. K. Chan, H. Yu, H. Jiang, *Nat. Commun.* **2014**, *5*, 3140.  
 [26] J. J. Adams, E. B. Duoss, T. F. Malkowski, M. J. Motala, B. Y. Ahn, R. G. Nuzzo, J. T. Bernhard, J. A. Lewis, *Adv. Mater.* **2011**, *23*, 1335.  
 [27] B. Y. Ahn, E. B. Duoss, M. J. Motala, X. Guo, S.-I. Park, Y. Xiong, J. Yoon, R. G. Nuzzo, J. A. Rogers, J. A. Lewis, *Science* **2009**, *323*, 1590.  
 [28] Z. Yan, F. Zhang, F. Liu, M. Han, D. Ou, Y. Liu, Q. Lin, X. Guo, H. Fu, Z. Xie, M. Gao, Y. Huang, J. Kim, Y. Qiu, K. Nan, J. Kim, P. Gutruf, H. Luo, A. Zhao, K.-C. Hwang, Y. Huang, Y. Zhang, J. A. Rogers, *Sci. Adv.* **2016**, *2*, e1601014.  
 [29] S. Xu, Z. Yan, K.-I. Jang, W. Huang, H. Fu, J. Kim, Z. Wei, M. Flavin, J. McCracken, R. Wang, A. Badea, Y. Liu, D. Xiao, G. Zhou, J. Lee, H. U. Chung, H. Cheng, W. Ren, A. Banks, X. Li, U. Paik, R. G. Nuzzo, Y. Huang, Y. Zhang, J. A. Rogers, *Science* **2015**, *347*, 154.  
 [30] Y. H. Zhang, S. D. Wang, X. T. Li, J. A. Fan, S. Xu, Y. M. Song, K. J. Choi, W. H. Yeo, W. Lee, S. N. Nazaar, B. W. Lu, L. Yin, K. C. Hwang, J. A. Rogers, Y. Huang, *Adv. Funct. Mater.* **2014**, *24*, 2028.  
 [31] Y. Zhang, S. Xu, H. Fu, J. Lee, J. Su, K. C. Hwang, J. A. Rogers, Y. Huang, *Soft Matter* **2013**, *9*, 8062.  
 [32] X. Yu, W. Huang, M. Li, T. M. Comberiate, S. Gong, J. E. Schutt-Aine, X. Li, *Sci. Rep.* **2015**, *5*, 9661.  
 [33] W. Huang, X. Yu, P. Froeter, R. Xu, P. Ferreira, X. Li, *Nano Lett.* **2012**, *12*, 6283.  
 [34] J.-H. Lee, C. Y. Koh, J. P. Singer, S.-J. Jeon, M. Maldovan, O. Stein, E. L. Thomas, *Adv. Mater.* **2014**, *26*, 532.  
 [35] M. Schumann, T. Bueckmann, N. Gruhler, M. Wegener, W. Pernice, *Light: Sci. Appl.* **2014**, *3*, e175.  
 [36] Z. Fan, H. Razavi, J.-W. Do, A. Moriwaki, O. Ergen, Y.-L. Chueh, P. W. Leu, J. C. Ho, T. Takahashi, L. A. Reichertz, S. Neale, K. Yu, M. Wu, J. W. Ager, A. Javey, *Nat. Mater.* **2009**, *8*, 648.  
 [37] P. V. Braun, *Chem. Mater.* **2014**, *26*, 277.  
 [38] G. M. Gratson, M. J. Xu, J. A. Lewis, *Nature* **2004**, *428*, 386.

- [39] J. A. Lewis, J. E. Smay, J. Stuecker, J. Cesarano, *J. Am. Ceram. Soc.* **2006**, *89*, 3599.
- [40] J. A. Lewis, *Adv. Funct. Mater.* **2006**, *16*, 2193.
- [41] C. Ladd, J.-H. So, J. Muth, M. D. Dickey, *Adv. Mater.* **2013**, *25*, 5081.
- [42] W. Zheng, H. O. Jacobs, *Adv. Funct. Mater.* **2005**, *15*, 732.
- [43] N. B. Crane, O. Onen, J. Carballo, Q. Ni, R. Guldiken, *Microfluid. Nanofluid.* **2013**, *14*, 383.
- [44] Y. Klein, E. Efrati, E. Sharon, *Science* **2007**, *315*, 1116.
- [45] J. Kim, J. A. Hanna, M. Byun, C. D. Santangelo, R. C. Hayward, *Science* **2012**, *335*, 1201.
- [46] S. Zhu, T. Li, *ACS Nano* **2014**, *8*, 2864.
- [47] S. Zhu, T. Li, *J. Phys. D: Appl. Phys.* **2013**, *46*, 075301.
- [48] J. Fischer, M. Wegener, *Laser Photonics Rev.* **2013**, *7*, 22.
- [49] K. A. Arpin, A. Mihi, H. T. Johnson, A. J. Baca, J. A. Rogers, J. A. Lewis, P. V. Braun, *Adv. Mater.* **2010**, *22*, 1084.
- [50] H. Li, X. Guo, R. G. Nuzzo, K. Jimmy Hsia, *J. Mech. Phys. Solids* **2010**, *58*, 2033.
- [51] C. Py, P. Reverdy, L. Doppler, J. Bico, B. Roman, C. N. Baroud, *Phys. Rev. Lett.* **2007**, *98*, 156103.
- [52] X. Y. Guo, H. Li, B. Y. Ahn, E. B. Duoss, K. J. Hsia, J. A. Lewis, R. G. Nuzzo, *Proc. Natl. Acad. Sci. USA* **2009**, *106*, 20149.
- [53] O. G. Schmidt, K. Eberl, *Nature* **2001**, *410*, 168.
- [54] S. Pandey, E. Gultepe, D. H. Gracias, *J. Visualized Exp.* **2013**, e50022.
- [55] X. Xu, H. Zhang, L. Zhang, Z. Wang, Y. Jiang, Z. Wu, *J. Phys. Chem. C* **2009**, *113*, 4634.
- [56] X. Li, *J. Phys. D: Appl. Phys.* **2008**, *41*, 193001.
- [57] Z. Wei, Z. Jia, J. Athas, C. Wang, S. R. Raghavan, T. Li, Z. Nie, *Soft Matter* **2014**, *10*, 8157.
- [58] O. G. Schmidt, C. Deneke, Y. M. Manz, C. Muller, *Phys. E* **2002**, *13*, 969.
- [59] J. H. Na, A. A. Evans, J. Bae, M. C. Chiappelli, C. D. Santangelo, R. J. Lang, T. C. Hull, R. C. Hayward, *Adv. Mater.* **2015**, *27*, 79.
- [60] E. T. Filipov, G. H. Paulino, T. Tachi, *Proc. R. Soc. A* **2016**, *472*, 20150607.
- [61] Y. Xia, G. Cedillo-Servin, R. D. Kamien, S. Yang, *Adv. Mater.* **2016**, *28*, 9637.
- [62] E. T. Filipov, T. Tachi, G. H. Paulino, *Proc. Natl. Acad. Sci. USA* **2015**, *112*, 12321.
- [63] W. J. Arora, A. J. Nichol, H. I. Smith, G. Barbastathis, *Appl. Phys. Lett.* **2006**, *88*, 053108.
- [64] J. S. Randhawa, T. G. Leong, N. Bassik, B. R. Benson, M. T. Jochmans, D. H. Gracias, *J. Am. Chem. Soc.* **2008**, *130*, 17238.
- [65] S. Pandey, M. Ewing, A. Kunas, N. Nguyen, D. H. Gracias, G. Menon, *Proc. Natl. Acad. Sci. USA* **2011**, *108*, 19885.
- [66] X. Li, *Adv. Opt. Photonics* **2011**, *3*, 366.
- [67] M. H. Huang, F. Cavallo, F. Liu, M. G. Lagally, *Nanoscale* **2011**, *3*, 96.
- [68] D. Bishop, F. Pardo, C. Bolle, R. Giles, V. Aksyuk, *J. Low Temp. Phys.* **2012**, *169*, 386.
- [69] Z. Yan, F. Zhang, J. Wang, F. Liu, X. Guo, K. Nan, Q. Lin, M. Gao, D. Xiao, Y. Shi, Y. Qiu, H. Luan, J. H. Kim, Y. Wang, H. Luo, M. Han, Y. Huang, Y. Zhang, J. A. Rogers, *Adv. Funct. Mater.* **2016**, *26*, 2629.
- [70] K. Nan, H. Luan, Z. Yan, X. Ning, Y. Wang, A. Wang, J. Wang, M. Han, M. Chang, K. Li, Y. Zhang, W. Huang, Y. Xue, Y. Huang, Y. Zhang, J. A. Rogers, *Adv. Funct. Mater.* **2016**, *27*, 1604281.
- [71] Y. Zhang, Z. Yan, K. Nan, D. Xiao, Y. Liu, H. Luan, H. Fu, X. Wang, Q. Yang, J. Wang, W. Ren, H. Si, F. Liu, L. Yang, H. Li, J. Wang, X. Guo, H. Luo, L. Wang, Y. Huang, J. A. Rogers, *Proc. Natl. Acad. Sci. USA* **2015**, *112*, 11757.
- [72] Y. Liu, Z. Yan, Q. Lin, X. Guo, M. Han, K. Nan, K. C. Hwang, Y. Huang, Y. Zhang, J. A. Rogers, *Adv. Funct. Mater.* **2016**, *26*, 2909.
- [73] D. Mark, S. Haeberle, G. Roth, F. von Stetten, R. Zengerle, *Chem. Soc. Rev.* **2010**, *39*, 1153.
- [74] C. D. Chin, V. Linder, S. K. Sia, *Lab Chip* **2012**, *12*, 2118.
- [75] P. P. Absil, J. V. Hryniewicz, B. E. Little, P. S. Cho, R. A. Wilson, L. G. Joneckis, P. T. Ho, *Opt. Lett.* **2000**, *25*, 554.
- [76] P. Froeter, X. Yu, W. Huang, F. Du, M. Li, I. Chun, S. H. Kim, K. J. Hsia, J. A. Rogers, X. Li, *Nanotechnology* **2013**, *24*, 475301.

Received: January 12, 2017  
Revised: February 20, 2017  
Published online: May 10, 2017